Adjacency effect estimation by ground spectra measurement and satellite optical sensor synchronous observation data

Jianwen Ma (马建文)[1,2] and Xue Chen (陈 雪)[1,2,3]

[1]*State Key Laboratory of Remote Sensing Science, Beijing*
[2]*Institute of Remote Sensing Applications, Chinese Academy of Sciences, Beijing 100101*
[3]*School of Geography, Beijing Normal University, Beijing 100875*

Received December 29, 2005

This paper addresses the estimation of adjacency effect of CBERS-2 image. The adjacency effect influences the digital number (DN) value of a pixel by adding surrounding scattering signals and path scattering signals. Based on the theory of radiation transfer model, a procedure is designed to measure the reflectance from the surface target materials and the materials in a box, which is 1.5 m above the surface to avoid upwelling reflectance. The results show that the adjacency effect varies from visible, near infrared and becomes steady within short infrared wavelength region; the adjacency effect weakens with the increase of distance between testing sites. The adjacency effect of CBERS-2 image is corrected and the quality of the resulting image is improved.

OCIS codes: 290.4210, 110.4850, 110.2990, 120.4820.

The adjacency effect is considered as the major correction procedure after the atmosphere and BRDF corrections. The main difficulty is in the quantitative measurement and estimation of the uncertainty components of adjacent influence[1−3]. This paper introduces recent work on adjacency effect including ground spectrum measurement and adjacency effect identification on CBERS-2 image.

According to radiation transfer model, when only the direct solar radiation illuminates a surface without atmosphere interfering, the target absorbs a fraction of the incoming photons, the remaining photons are reflected back to the space. The radiance measured by the satellite directly depends upon the target properties. In fact, a part of sunlight reflected by adjacency areas is scattered to the target. It becomes part of radiance captured by the sensor. The phenomenon is called adjacent effect, which blurs the image[4,5]. For a non-uniform surface, adjacency effect is weak to 1 km or lower spatial resolution and it can be neglected. As a result, dark pixels look brighter and bright pixels look darker. Especially when the spatial resolution is higher than 500 m the adjacent effect correction should be considered.

Adjacency effect models can be summarized into two groups: 1) developing empirical formulae based on radiation transfer model and 2) using the atmospheric point spread function (PSF). The radiation transfer integral-differential equation does not have strict practical solutions[6], different empirical formulae on adjacency effect have been got with different conditional approximations[7−10]. Items in those algorithms are not straightforward, or they are too complicated due to large amount of atmospheric parameters. PSF methods including image target method[11,12], Monte-Carlo or optimization algorithm simulation[13,14], geometrical optics computation[15], and radiation transfer simulation[16]. Those results rely on specific image information and have a large random error; or they are computationally expensive. Moreover, the two classes of models have a common defect: neither of them is combined with ground spectra measurement.

Ground spectra measurement methods are designed based on the principle of radiation transfer model. Figure 1(a) illustrates that the illumination of the target is the combination of two kinds of lights which are directly transmitted sunlight, and the scattering light after interacting with surrounding areas, that is, the analytical spectral device (ASD) collects light from areas ① and ②. The designed platform box above 1.5 m of the target prevents scattering lights from adjacent areas, ASD=①, see Fig. 1(b). The platform box is about 0.5×0.5 (m) in area, 0.15×0.15 (m) in height.

On May 4, 2004, we carried out fieldwork in Guanting (N40°17′, E115°41′). Water, grassland and sands

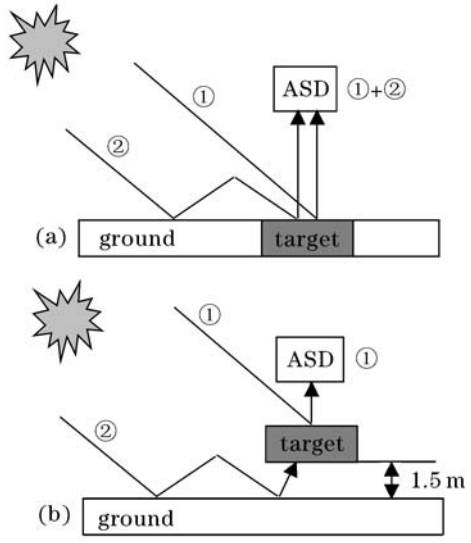

Fig. 1. Principle of the ground adjacency effect measurements.

are selected. At each sampling site, ground target spectra and sample spectra on a platform box are measured. Five times reflectance data are collected and the average reflectance curves are outputted. When beginning each measurement of the target and the platform, the reference panel is initialized for the ASD with the spectrum range from 350 to 2500 nm. The wavelength interval is 1 nm. The detector is operated at 0.2-m height in the nadir direction. Ground measurements are arranged in the period times of CBERS-2 overpass. The proportions of minerals in desert sand are 65% quartz, 30% feldspar, and 5% hornblende.

The results show that the reflectance curves of target and platform have some difference in both desert and grassland sites, see Fig. 2. Compared with ground measurement results, the sample reflectance curves on the platform are lower; moreover, differences between target sand/grass spectra curves and platform box sand/grass spectra increase from visible, near infrared to short wavelength infrared region.

There are three major kinds of radiance captured by the sensor: 1) the radiance directly transmitted from the target to the sensor, 2) the atmospheric aerosol scattering radiation which has not interacted with the ground, and 3) the radiance reflected from the surroundings of the target and then scattered into the view field of the sensor.

The exoatmospheric reflectance ρ^* is composed of three parts, atmospheric intrinsic reflectance $\rho_{\rm a}$, target pixel reflectance $\rho_{\rm t}$, and background reflectance $\rho_{\rm b}$[17],

$$\rho^* = \rho_{\rm a} + T(\theta_v)\left(\rho_{\rm t}\iint_{\rm target}\mathrm{PSF}(x,y)\,\mathrm{d}x\mathrm{d}y + \rho_{\rm b}\iint_{\rm background}\mathrm{PSF}(x,y)\mathrm{d}x\mathrm{d}y\right), \quad (1)$$

where $T(\theta_v)$ is the total transmittance from the surface to the sensor and PSF is the atmospheric point spread function. Background reflectance $\rho_{\rm b}$ is given by

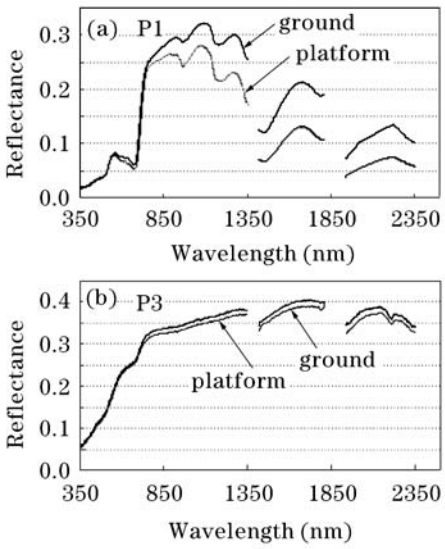

Fig. 2. Grassland (a) and desert sand (b) spectra curves of target and platform box.

$$\rho_{\rm b}(x,y) = \frac{\sum_{j=-n}^{n}\sum_{i=-n}^{n}\rho_1(x,y)\exp(-r)}{\sum_{j=-n}^{n}\sum_{i=-n}^{n}\exp(-r)}, \quad (2)$$

where ρ_1 is the surface reflectance neglecting adjacency effect, n corresponds to the number of pixels for the selected range of adjacency effect. Slater indicated that the radius of the adjacency effects ranges from 10 m off the borders under zero-turbidity conditions, through 100 m off the borders under normal turbidity conditions, and up to 1 km off the target's boundary under highly turbid conditions[18]. n should be determined according to Slater's conclusion and the spatial resolution of the sensor. The increase of n does not change background reflectance greatly after n reaches a certain degree. The calculation of $\rho_{\rm b}$ does not include (0,0) pixel, which is the target pixel. Here ρ_1 is used instead of target pixel reflectance $\rho_{\rm t}$ since the latter is not available, and the error introduced can be reduced by using successive iterations[19].

In the case of the value is 1 only when integrating PSF over the full spatial ranges so as to let $\iint_{\rm target}\mathrm{PSF}(x,y)\mathrm{d}x\mathrm{d}y = \alpha$ $(0<\alpha<1)$, then $\iint_{\rm background}\mathrm{PSF}(x,y)\mathrm{d}x\mathrm{d}y = 1-\alpha$. Equation (1) can be rewritten as

$$\rho^* = \rho_{\rm a} + T(\theta_v)\left(\rho_{\rm t}\alpha + \rho_{\rm b}(1-\alpha)\right). \quad (3)$$

After atmospheric intrinsic reflectance and extinction removed, the surface reflectance neglecting adjacency effect ρ_1 can then can be written as

$$\rho_1 = \rho_{\rm t}\alpha + \rho_{\rm b}(1-\alpha). \quad (4)$$

Because of $0<\alpha<1$, if $\rho_{\rm t}\neq\rho_{\rm b}$, the value of ρ_1 is between $\rho_{\rm t}$ and $\rho_{\rm b}$. Therefore, as a result of adjacency effect, dark pixels look brighter and bright pixels look darker, resulting in images look hazy and lack contrast. Here α is defined as the $\rho_{\rm t}$ contribution proportion to ρ_1, which reflects adjacency effect intensity.

The radiometric calibration assigns to each digital number (DN), the corresponding at-sensor radiance L (unit: $\mathrm{W\cdot m^{-2}\cdot\mu m^{-1}}$) is

$$L(k) = c_0(k) + c_1(k)\,\mathrm{DN}(k), \quad (5)$$

where k refers the band number, and c_0, c_1 are the calibration coefficients of offset and gain.

For a flat, Lambertian surface under a horizontally homogeneous atmosphere, the exoatmospheric reflectance ρ^* can be expressed as

$$\rho^* = \frac{\pi L d^2}{E_{\rm s}\cos\theta_{\rm s}}, \quad (6)$$

where $E_{\rm s}$ is the mean solar flux at the top of the atmosphere, $\theta_{\rm s}$ is the solar zenith angle, the factor d^2 accounts for the sun-earth distance (d is in astronomical units)

$$d = \frac{1}{1-0.01674\cos[0.9856(\mathrm{JD}-4)]}, \quad (7)$$

where JD is the Julian day on which satellite overpasses. A 3.5% variation of d exists in a year.

There is a relationship between ρ^* and ρ_1

$$\rho^* = \rho_a + \frac{\rho_1}{1-\rho_1 S} T(\theta_s) T(\theta_v), \tag{8}$$

where S is spherical albedo of atmosphere, $T(\theta_s)$ and $T(\theta_v)$ are the total transmittance from the surface to the sun and sensor.

Thus ρ_1 is retrieved from image as

$$\rho_1 = \frac{\rho^* - \rho_a}{T(\theta_s) T(\theta_v) + (\rho^* - \rho_a) S}. \tag{9}$$

Among parameters needed in calculation, c_0, c_1 are provided by CRESDA, θ_s is in the head file of remote sensing image, E_s can be found in Ref. [20], and S, $T(\theta_s)$, $T(\theta_v)$ are obtained by running 6S software.

Comparison between the retrieved CBERS-2 reflectance and the measured reflectance is shown in Fig. 3. Measured reflectance is the aggregated ASD measurement result using the CBERS-2 sensor spectral response functions in 6S software for each band. Because band 5 is a panchromatic band, only the data of the charge-coupled device (CCD) 1—4 bands were selected.

Ideally, points in Fig. 3 should be perfectly matched and they should be all in the $y = x$ line. If there is no adjacent effect, the points should be distributed closely around the $y = x$ diagonal line. In our case, due to the existence of adjacent effect, bright pixels tend to be darker and dark pixels tend to be brighter. Thus the points are distributed around lines whose slopes are less than 1 and whose intercepts are bigger than 0. For a set of data of a band, total deviation $\sum \left((\rho_{\text{measure}} - \rho_1)/\rho_{\text{measure}}\right)^2$ is used to measure surface reflectance changes caused by adjacency effect. The total deviations of CCD 1—4 bands are 1.83, 1.27, 1.24, 0.72, which indicates that from CCD1 to CCD4, the distribution of the points is closer to the $y = x$ line and the adjacency effect becomes weaker.

Retrieved surface reflectance ρ_{img} after adjacency effect correction is

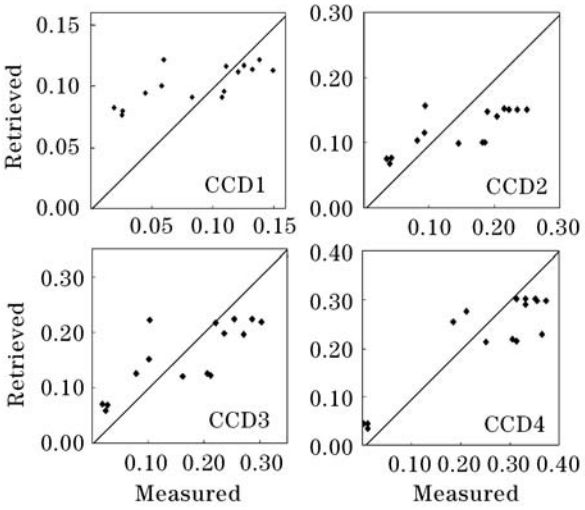

Fig. 3. Comparison of the retrieved reflectance and the measured reflectance.

$$\rho_{\text{img}} = \frac{\rho_1 - \rho_b (1-\alpha)}{\alpha}. \tag{10}$$

The question lies in how to obtain appropriate α value to make ρ_{img} of all points as close as possible to ρ_{measure} simultaneously for a band, or to make the point distribution as close as possible to the $y = x$ line. Here an "inverse" least square method (LSM) is adopted. In LSM, points are known, and the linear relationship $y = x$ is remained to be obtained. While in our method the linear relationship $y = x$ is assured, and point locations are unfixed. When the total deviation F is the least, α is the result by inputting diverse α. Here ρ_{img} is the most close to ρ_{measure} as a whole.

During calculation, n is set to 30 when computing background reflectance in Eq. (10), the range of α is set to [0.01,0.99], and the step size is 0.01. The α results of CCD 1—4 bands are respectively 0.77, 0.83, 0.86, 0.91. The results show that from CCD 1 to CCD 4 the contribution proportion of the target pixel increases, and the adjacency effect decreases.

Among the three components of the exoatmospheric reflectance ρ^*, atmospheric intrinsic reflectance ρ_a is independent of surface reflectance and target pixel reflectance ρ_t essentially depends upon the reflectance of the target pixel, and background reflectance ρ_b depends upon the reflectance of adjacent pixels. The adjacency effects in three different cases are shown in Fig. 4. The same CCD pixel is surrounded by three kinds of infinitesimal background situations. 1) Background darker than the target ($\rho_t = 0.4$, $\rho_b = 0.2$, Fig. 4(a)), 2) uniform surface, same reflectance of the target and its environment ($\rho_t = \rho_b = 0.4$, Fig. 4(b)), and 3) background brighter than the field ($\rho_t = 0.4$, $\rho_b = 0.6$, Fig. 4(c)). Each reflectance is invariable in different bands.

In the three cases, ρ_a, ρ_t are equal due to the same atmospheric conditions and target pixels. Because of the existence of adjacency effect, different backgrounds lead to different ρ_b, consequently different ρ^*. In Fig. 4(d), three ρ^* tend to be consistent from band 1 to band 4, and adjacency effect decreases. In Fig. 4(d), the target pixel is the same to its background in ρ^*(b). ρ^*(b) is generated by a uniform surface, and adjacency effect does not introduce disturbance information. When the target pixel is brighter than background ($\rho_t > \rho_b$), ρ^*(a) < ρ^*(b), and the target looks darker in the image; while when the target pixel is darker than background ($\rho_t < \rho_b$), ρ^*(c) > ρ^*(b), and the target looks brighter in the image.

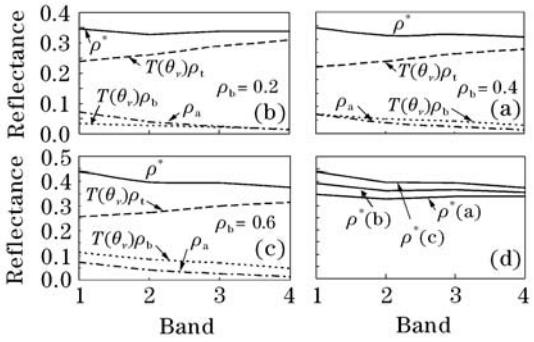

Fig. 4. Adjacency effect in different bands. The target reflectance $\rho_t = 0.4$.

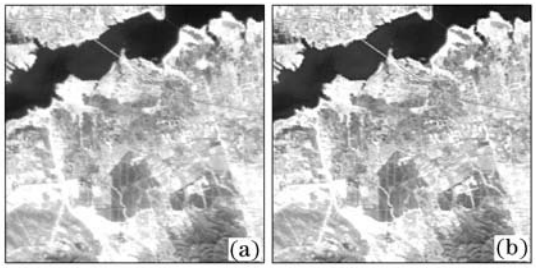

Fig. 5. CCD2 image before (a) and after (b) adjacency effect correction.

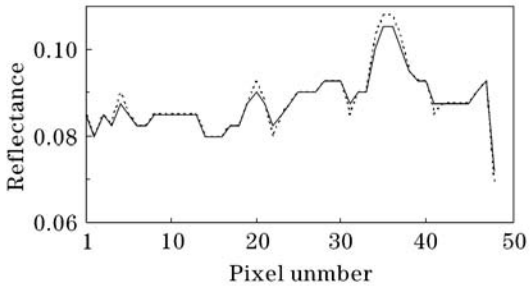

Fig. 6. Reflectance profiles before (solid line) and after (dashed line) correction.

The surface reflectance neglecting adjacency effect ρ_1 is derived form the CBERS-2 image in this research, and the surface reflectance after adjacency effect correction ρ_{img} is derived. Figure 5 shows the comparison between CBERS-2 CCD2 band images before and after adjacency effect correction. After adjacency effect correction, the contrast increases and the details are enhanced. Originally fine dark regions circled by bright pixels are blurry. Their detail visibilities increase markedly after correction. Figure 6 shows the profiles before and after correction.

In conclusion, this paper introduces an adjacency effect measurement and estimate scheme on ground spectra measurement and satellite synchronous observation data, including a two-dimensional (2D) Gaussian PSF model analysis. The results show that the adjacency effect varies from visible, near infrared and becomes steady within short wavelength region, while adjacency effect of pixels of satellite data becomes weaker from visible, near infrared to short wavelength infrared region because of atmosphere scattering influences. The adjacency effect weakens with the increase of distance between spectra measurement sites. The new adjacency effect correction method is applied to CBERS-2 image, and the image quality is improved. For the CBERS-2 image pixel adjacent effect estimation and correction procedure introduced in the paper it only assumes a Lambertian surface and is based on radiation transfer model. The algorithm can also be applied to other kinds of satellite images.

This work was supported by the National Natural Science Foundation of China under Grant No. 40371086. J. Ma's e-mail address is jianwen@irsa.ac.cn.

References

1. L. Bastin, P. F. Fisher, and J. Wood, Computers and Geosciences **28,** 337 (2002).
2. C. Feng, J. Ma, Q. Dai, and X. Chen, in *Proceedings of IEEE 2004 International Geoscience and Remote Sensing System Symposium* (IGARSS'04) 7IWE_21_04 (2004).
3. J. Ma, X. Li, C. Feng, and X. Chen, IEEE Trans. Geoscience and Remote Sensing **44,** 729 (2006).
4. Y. J. Kaufman and C. Sendra, International J. Remote Sensing **9,** 1357 (1988).
5. L. C. Sanders, J. R. Schott, and R. Raqueño, Remote Sensing of Environment **78,** 252 (2001).
6. X. Xu and P. Wang, J. Remote Sensing (in Chinese) **4,** 268 (1999).
7. Y. J. Kaufman, Appl. Opt. **23,** 4164 (1984).
8. E. F. Vermote, D. Tanre, J. L. Deuze, M. Herman, and J.-J. Morcette, IEEE Trans. Geosciences and Remote Sensing **35,** 675 (1997).
9. K. Thome, F. Palluconi, T. Takashima, and K. Masuda, IEEE Trans. Geosciences and Remote Sensing **36,** 1199 (1998).
10. S. Liang, H. Fang, and M. Chen, IEEE Trans. Geoscience and Remote Sensing **39,** 2490 (2001).
11. C. P. Ruiz and F. J. A. López, International J. Remote Sensing **23,** 2379 (2002).
12. Z. Liu, C. Wang, and C. Luo, J. Remote Sensing (in Chinese) **8,** 234 (2004).
13. P. N. Reinersman and K. L. Carder, Appl. Opt. **34,** 4453 (1995).
14. B. Cong, in *Proceedings of the International Conference on Information Technology: Coding and Computing* (ITCC'00) 344 (2000).
15. C. C. Borel and S. A. Gerstl, Proc. SPIE **1688,** 620 (1992).
16. D. Lu and M. Duan, in *Proceedings of Asian Conference on Remote Sensing* (ACRS) (1999).
17. R. Richter, International J. Remote Sensing **18,** 2827 (1997).
18. P. N. Slater, *Remote Sensing, Optics and Optical Systems* (Addison-Wesley, London, 1980).
19. M. Putsay, International J. Remote Sensing **13,** 1549 (1992).
20. G. Chander and B. Markham, IEEE Trans. Geosciences and Remote Sensing **41,** 2674 (2003).